CMOS Integrated Antenna-Coupled Field-Effect Transistors for the Detection of Radiation From 0.2 to 4.3 THz

Sebastian Boppel, Alvydas Lisauskas, Martin Mundt, Dalius Seliuta, Linas Minkevičius, Irmantas Kašalynas, *Member, IEEE*, Gintaras Valušis, Martin Mittendorff, Stephan Winnerl, Viktor Krozer, *Senior Member, IEEE*, and Hartmut G. Roskos

Abstract—This paper reports on field-effect-transistor-based terahertz detectors for the operation at discrete frequencies spanning from 0.2 to 4.3 THz. They are implemented using a 150-nm CMOS process technology, employ self-mixing in the n-channels of the transistors and operate well above the transistors' cutoff frequency. The theoretical description of device operation by Dyakonov and Shur is extended in order to describe the device impedance, responsivity, and noise-equivalent power for a novel detection concept, which couples the signal to the drain. This approach enables quasi-static (QS) detection and calibration of the detectors. The different transport regimes (i.e., QS, distributed resistive, and plasmonic mixing) and their transitions are theoretically discussed and experimentally accessed. Responsivity values of 350 V/W at 595 GHz, 30 V/W at 2.9 THz, and 5 V/W at 4.1 THz are reported. At 0.595 THz, we determine the optical noise equivalent power (NEP) to be 42 pW/$\sqrt{\text{Hz}}$; at 2.9 THz, the value is 487 pW/$\sqrt{\text{Hz}}$. All values are reported for optimum gate bias with respect to NEP at 295 K. For 0.595 THz, theory predicts a NEP value at threshold as low as 2 pW/$\sqrt{\text{Hz}}$ for ideal coupling of the radiation.

Index Terms—CMOS, direct terahertz detection, distributed resistive self-mixing, patch antennas, plasmonic detection, submillimeter-wave detectors, terahertz detectors.

I. INTRODUCTION

COMMON knowledge suggests that efficient operation of field-effect transistors (FETs) above their cutoff frequency is not feasible. While this is true for transit-time-limited applications such as power amplification and logic switching operations, density waves of charge carriers (plasma waves) relax this limitation when rectifying and mixing phenomena are considered. Plasma waves in 2-D electron gases and their interaction with electromagnetic waves have been the subject of intensive theoretical and experimental studies for over three decades [2] In 1996, Dyakonov and Shur suggested utilizing the excitation of plasma waves in the transistors' channels for the detection and mixing at frequencies higher than the cutoff frequency, thus paving the way for novel devices for the terahertz frequency range [3]. The viability of this approach was proven soon after with experiments on a GaAs high electron-mobility transistor (HEMT), which was used to detect radiation at 2.54 THz, 30 times above its transit-time-defined cutoff frequency [4]. Numerous studies with HEMTs at various temperatures and for different coupling schemes followed [5]–[11].

The focus of this paper is on terahertz detection with silicon MOSFETs. Such devices, without antenna or grating couplers, were first investigated in 2006 by the Knap group of Montpellier with radiation at 700 GHz [12]. At room temperature, where the measurements were performed, plasma waves are strongly attenuated and can only propagate through a part of the FET's channel. Since the attenuation prevents standing plasma waves to occur in the channel, this situation was termed the "non-resonant case" of the theory of Dyakonov and Shur [13]. This case can also be understood as a close relative of the well-known "resistive mixing" with FETs. If the frequency is increased, resistive mixing develops into "distributed resistive self-mixing," where the channel of the FET can no longer be treated as a lumped element, but rather as a ultra-high-frequency waveguide [14].

The practical interest in MOSFET-based terahertz detectors and mixers strongly increased, after the first antenna-coupled MOSFET detectors and few-pixel focal plane arrays were implemented successfully for 645 GHz using a 250-nm CMOS foundry process, which did not need to be supplemented by additional fabrication steps [14], [15]. Device performance was further improved by various means such as the use of a more advanced 65-nm SOI process technology [16] or by modified circuit concepts in combination with cost-efficient 130- or 150-nm CMOS technology, respectively [17], [18]. Typical performance data, presented in [18] for 590-GHz detectors, are an optical noise-equivalent power (NEP) of 43 pW/$\sqrt{\text{Hz}}$ and a maximum (capacitive loading limited) optical responsivity of 970 V/W (both values averaged over a number of individual
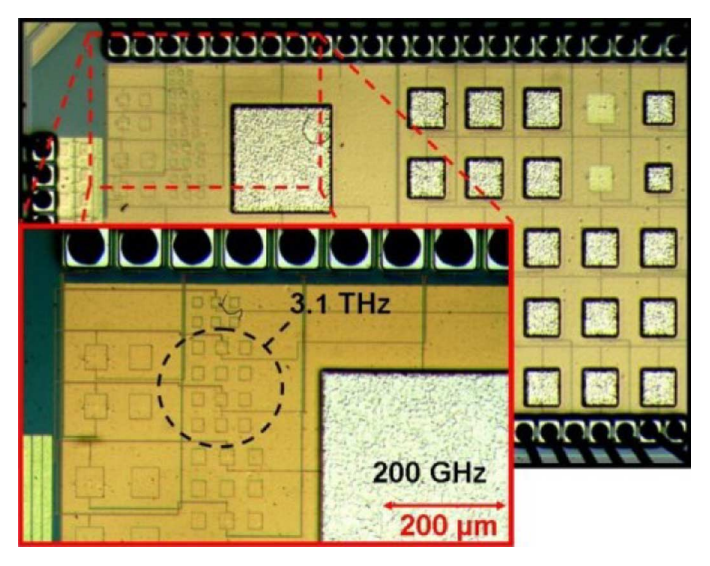
Fig. 1. Micrograph of a 1.5×2.5 mm^2 large silicon die showing different patch antennas for ten different terahertz frequencies. A close-up photograph shows the high-frequency section (for frequencies larger than 1.4 THz) of the chip, as well as a part of a 200-GHz antenna.
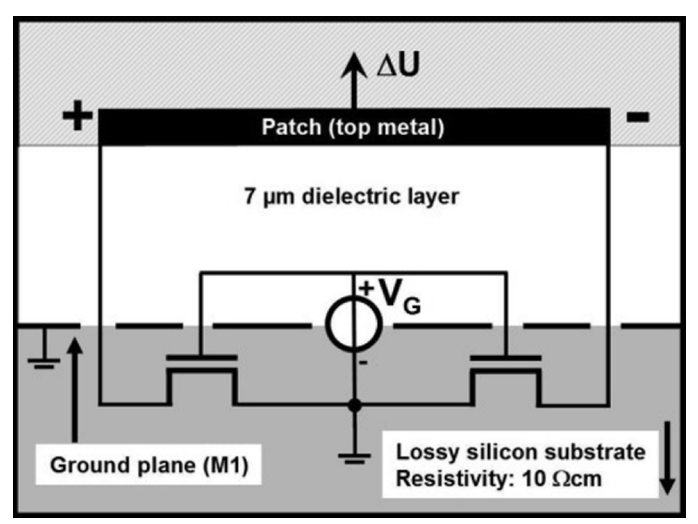

Fig. 2. Schematic cross section of a patch-antenna-coupled pair of FETs for the detection at 590 GHz (dimensions not to scale). The antenna is also used for signal readout. V_g: external gate bias voltage.

devices), an excellent uniformity, low inter-chip variation of less than 8% among pixels, and a high fabrication yield. The good performance strongly suggests that CMOS detectors are suitable candidates for commercial terahertz cameras applicable to imaging in fields such as nondestructive testing, quality control, medicine, and security [19]. In fact, a 1-kpixel and a 144-pixel focal-plane array, the latter also suitable for heterodyne operation, have recently been implemented and tested at frame rates well above 1 frame/s [20], [21].

Much of the recent work on MOSFET terahertz detectors is focused on the sub-1-THz frequency range. In this paper, we explore operation at higher frequencies and systematically study detection of free-space radiation from 0.2 to 4.3 THz. We exploit the novel detector concept of [18], where the signal received by the antenna is applied between the drain and source terminals. This approach allows for ready detector calibration by measurements of low-frequency signals. In Section II, we provide details on design and implementation of the devices. Sections III–V present the theoretical approach for the description of detector operation, based on the Dyakonov–Shur model, and provide simulation data for different gate-bias voltage regimes, considering device impedance, responsivity, and NEP. The three frequency regimes of quasi-static (QS) mixing, distributed resistive self-mixing, and nonresonant plasmonic mixing, are distinguished from each other. Section VI presents experimental results demonstrating sensitive detection at frequencies up to 4.3 THz, covering all three frequency regimes. Theoretical and experimental data are compared.

II. DETECTOR DESIGN AND LAYOUT

Detectors for ten different resonance frequencies spanning from 200 GHz to 4.3 THz were implemented on a 1.5×2.5 mm^2 large silicon die (see Fig. 1) using the 150-nm CMOS process provided by LFoundry GmbH. Each detector consists of a monolithically integrated differential patch antenna connected to a pair of transistors acting as rectifying

elements. Low-leakage transistors with a 150-nm channel length and a 320-nm gate width are used. The transistor cutoff frequency is approximately 35 GHz at threshold.

Fig. 2 illustrates the design of a 590-GHz detector. The radiation (with its polarization vector in the paper plane) is received by a patch antenna located at the top of the insulation layer of the circuit back-end. From both edges of the patch, terahertz signals are guided downwards vertically to two MOSFETs, which correspondingly are fed with signals of opposing signs. The feeds are realized as vias. In contrast to earlier device implementations described in [14] and [15], the terahertz signals are coupled to the drain terminals of the MOSFETs. The transistors rectify the signals, with each transistor generating a dc source–drain voltage, which is ready for readout through the center of the antenna patch. Note that the transistors do not operate in a differential way, there is no subtraction of signals involved. Two transistors instead of one are used because: 1) the antenna with its immediate vicinity (feeds) remains symmetrical, and thus, also the radiation pattern and 2) lossy high-frequency transmission lines can be avoided.

The rectified signal is read out at the center of the antenna against the dc ground connected to the source of the transistors. The gates and sources of both transistors are ac grounded, acting as an ac short between terminals. The gates are connected to an external source for applying a common dc gate bias voltage V_g. This design concept exhibits a couple of advantages. By reading out the detector at the antenna center (ac ground), the antenna itself acts as a low-pass filter, and therefore, additional lossy filter structures are avoided. Furthermore, and already aforementioned, the transistors are placed in proximity to the antenna feeds. Therefore, transmission-line losses are reduced. These changes and the avoidance of long transmission-line structures contribute to minimize performance variations, as we have reported in our earlier study [18], which used the same detector design. Another advantage of drain coupling in contrast to the gate coupling approach discussed by Dyakonov and Shur, and implemented in [14] and [15], is its suitability to detect low-frequency signals, which are applied electronically through the

readout terminal using a standard signal generator and a bias tee. Comparison of the measured rectified signal with the results of terahertz measurements allows the quantitative determination of high-frequency parasitic circuit effects and of the antenna-to-detector impedance mismatch at terahertz frequencies. With these parameters determined, low-frequency measurements can then be used for detector calibration, in order to correct performance variations of different pixels.

We avoid applying a dc bias to the drain, even though the responsivity can significantly be enhanced, because the noise also increases with the consequence that the signal-to-noise ratio can be improved at most by a small amount [22]. Furthermore, additional components such as amplifiers are avoided because they would add noise, which would make the study of the pure MOSFET devices with regard to the NEP more difficult.

Essential for highly sensitive detectors is an efficient coupling of the free-space radiation to the MOSFETs. The lossy silicon substrate with a resistivity of 10 Ωcm and the limited thickness of the back-end of standard CMOS technology complicate the design of on-chip antennas. The problem of losses in the silicon substrate can be avoided by using silicon-on-insulator (SOI) technology [16]. Due to the increased costs of the process technology, we discard this possibility in this contribution and rather follow the approach of [14] and [15] employing terahertz patch antennas whose ground planes prevent the radiation field from being exposed to the doped silicon substrate. A positive side effect of this choice is that patch antennas exhibit a relatively high impedance, which somewhat approaches the high device impedance of the MOSFET-based detectors (the latter being in the range of a few kΩ). The high transistor impedance results: 1) from the fact that the responsivity is highest close to the threshold voltage and 2) from the choice of a short channel width in order to reduce parasitic capacitances at terahertz frequencies.

The metal stack of the interconnect back-end of the standard CMOS process becomes highly functional for the implementation of the patch antennas. The LFoundry technology offers an approximately 7-μm-thick dielectric layer between metal layers "M1" defined as the lowest layer and the top layer "MT." While this yields a ratio of dielectric-layer thickness to effective wavelength of the radiation in the material of less than 1% for frequencies below 200 GHz, a ratio of 20% is reached at 4.3 THz. Which ratio is optimal for a specific detector depends on many aspects. Generally, one can say that the design constraints by the thickness of the dielectric layer relax with rising frequency and allow implementation of efficient antenna structures.

We fabricated groups of ten different detectors for discrete frequencies chosen to match various available radiation sources. Antenna frequencies below 600 GHz were tailored to our electronic sources, while frequencies above 600 GHz were tailored to meet the discrete emission lines of a CO_2-pumped molecular gas laser available in Vilnius. The scaling of the antenna area with the square of the wavelength becomes evident when the 200 GHz and the 3.1-THz antennas are compared in Fig. 1. Obviously, multipixel cameras would require significantly less chip space at higher frequencies.

Table I summarizes important geometrical data of the antennas, as well as simulation results for them (obtained with

TABLE I
ANTENNA SIMULATION PARAMETERS AND RESULTS FOR DETECTORS
IMPLEMENTED FOR DIFFERENT FREQUENCIES

Pixel	Patch size	Metal layer	Resonance frequency	Resonance impedance	Efficiency	Bandwidth
	μm^2		GHz	Ω	%	%
A*	321x375	MT	220	77	18	4.5
B*	241x281	MT	295	105	25	9.5
C	218x236	MT	320	143	27	10
D	109x118	MT	630	236	52	10.5
E	92x100	MT	735	250	60	12
F	45x49	M4	1475	177	46	10.5
G	36x40	M4	1810	187	55	12
H	23x26	M3	2770	100	40	15
I	19x21	M3	3290	105	48	17
J	15x16	M2	4330	41	26	22

CST Microwave Studio). The resonance frequency, impedance at resonance, radiation efficiency ϵ at resonance, and power radiation bandwidth are listed. Designs A and B are based on different patch geometries, which is indicated by the * symbol. Designs C to J are—as far as technology permitted—scaled modifications of the 590-GHz detector implementation of [18]. This approach was chosen in order to keep the devices as comparable to each other as possible. For smaller patch sizes, lower metal layers (M2 to MT) were used for the patch, taking the change of the dielectric environment of the patch into account in the simulations. While the area of the patch could be adjusted continuously, the separation of the patch and the ground plane, as well as the thickness of the patch metallization, could not, but were determined by the technology-given values. Especially at higher frequencies, the antenna performance can still be considerably optimized in the future.

III. HYDRODYNAMIC DESCRIPTION OF THE TRANSPORT

A fundamental theoretical description of the rectification phenomena in FETs has been given in the framework of a hydrodynamical theory in [3]. One finds several approximate treatments in the literature [3], [13]–[15], [23], where the authors introduce simplifications such as the parallel-plate charge-control model or the overdamped-plasmon approach, or the conditions at the drain are treated as open, i.e., the total current is set to be zero. In order to describe detector operation relevant for our design with the signal coupling conditions as shown in Fig. 2, and not to be limited by the above-mentioned simplifications, we return to the basic hydrodynamic description of electron transport, described by the equation of motion and the continuity equation, and follow the methods introduced in [3] for our specific situation. The two constitutive equations are

$$\frac{\partial v}{\partial t} + v\frac{\partial v}{\partial x} + \frac{e}{m}\frac{\partial U}{\partial x} + \frac{v}{\tau} = 0 \quad (1)$$

$$\frac{\partial n}{\partial t} + \frac{\partial nv}{\partial x} = 0 \quad (2)$$

with local drift velocity $v(x,t)$, local gate-to-channel voltage swing $U(x,t)$, location in channel x, time t, elementary charge

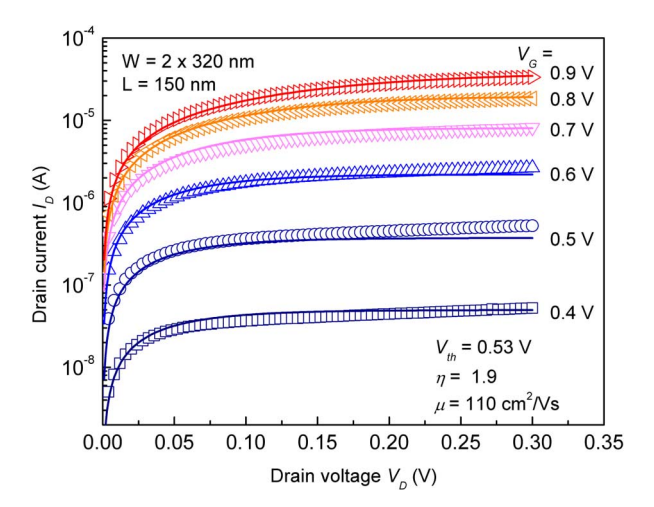| Symbol	Quantity	Symbol	Quantity
C_{ox}	Gate oxide capacitance per unit area	$v(x,t)$	Local drift velocity
e	Elementary charge	V_a	Voltage amplitude of external excitation
$f(\omega)$	Efficiency factor	V_D	Drain voltage
I_D	Drain current	V_G	Gate bias voltage
k	Wave vector	V_T	Thermal voltage
k_B	Boltzmann constant	V_{th}	Threshold voltage
L	Length of transistor	W	Width of transistor
m	Effective electron mass	x	Location in channel
$n(x,t)$	Local electron density	Z_d	Device impedance
NEP	Noise equivalent power		
R_d	Device resistance	ΔU	Detector signal
$\mathfrak{R}_I$	Current responsivity	ε	Radiation efficiency
s	Phase velocity	η	Subthreshold ideality factor
t	Time		
t_V	Voltage transfer	μ	Electron mobility
T	Temperature	τ	Scattering time
$U(x,t)$	Local gate-to-channel voltage swing	ω	Frequency of external excitation

Fig. 3. Points: measured stationary output characteristics of a nMOS transistor pair with 150-nm channel length and 320-nm width. Lines: fit by (4). The differential detector configuration (see Fig. 2) is taken into account by doubling the channel width in the fit procedure, which reflects the fact that, at dc measurement conditions, the configuration reduces to the parallel connection of two transistors.

e, effective mass m, and scattering time τ. All relevant parameters and constants used in the derivations are also summarized in Table II. The electron density n in the inversion layer can be described by a unified charge control model [24]

$$n = \frac{C_{ox}\eta V_T}{e} \ln\left(1 + \frac{1}{2}e^{(V_G - V_{th})/\eta V_T}\right) \quad (3)$$

with C_{ox} being the gate–oxide capacitance per unit area and V_G and V_{th} being the gate bias and threshold voltage, respectively; $V_T = k_B T/e$ is the thermal voltage, k_B is the Boltzmann constant, T is the temperature, and η is the so-called subthreshold ideality factor. By replacing the global V_G with the corresponding local gate-to-channel voltage swing $U(x,t)$, (3) describes the local charge carrier density as a function of the local voltage, assuming immediate response [3], [13].

As a first step, we derive the following expression for the drain current introduced by a fixed drain voltage V_D from (1) and (2), while taking (3) into account

$$I_D = \frac{\eta^2 V_T^2 \mu C_{ox} W}{L} \left[F_1\left(\frac{V_G - V_{th}}{\eta V_T} - \ln(2)\right) \\ - F_1\left(\frac{V_G - V_{th} - V_D}{\eta V_T} - \ln(2)\right) \right]. \quad (4)$$

Here, $\mu = e\tau/m$, W, and L denote electron mobility, transistor gate width, and length, correspondingly. We use the complete Fermi–Dirac integrals $F_n(x) = 1/\Gamma(n+1)\int_0^x t^n/(\exp(t-x)+1)\, dt$. Alternatively, the solution can be expressed in terms of the dilogarithm function $\mathrm{dilog}\, x = \int_1^x \ln t/(1-t)\, dt$ [25], which directly relates to the Fermi–Dirac integral for $n = 1$, i.e., $F_1(x) = -\mathrm{dilog}(1 + \exp(x))$. At high gate bias, i.e., $V_G - V_{th} \gg \eta V_T$, (4) simplifies to the well-known triode equation. We use (4) to determine values of η, μ, and V_{th} for the transistors used in our experiments. Fig. 3 shows experimentally measured FET output characteristics of one of

the previously described detectors together with fitted curves calculated with (4) using the following universal bias-independent fitting parameters: $\eta = 1.9$, $\mu = 110\ \mathrm{cm^2/V \cdot s}$, and $V_{th} = 0.53$ V. The measured data and the fitted curves exhibit good agreement. The extracted dc resistance also agrees well with measured resistances (data not shown). Only close to saturation does one finds slight deviations, which most likely are a result of the fact that the model neither includes diffusion currents, nor takes other aspects into account, which are important for short devices, e.g., channel narrowing or drain-induced barrier lowering [26].

IV. HARMONIC EXCITATION AND DEVICE IMPEDANCE

Now let us consider the external oscillatory excitation at frequency ω and voltage amplitude V_a (exact boundary conditions will be defined later). Let us search for the solutions of the oscillating gate-to-channel voltage, the electron velocity, and the carrier density written in the following forms:

$$U(x,t) = \bar{U} + \frac{1}{2}\left\{U_1 e^{i\omega t} + U_2 e^{i2\omega t} + \cdots\right\} + \text{c.c.} \quad (5)$$

$$v(x,t) = \bar{v} + \frac{1}{2}\left\{v_1 e^{i\omega t} + v_2 e^{i2\omega t} + \cdots\right\} + \text{c.c.} \quad (6)$$

$$n(x,t) = \bar{n} + \frac{1}{2}\left\{n_1 e^{i\omega t} + n_2 e^{i2\omega t} + \cdots\right\} + \text{c.c.} \quad (7)$$

Here, $\bar{U}$, $\bar{v}$ and $\bar{n}$ describe stationary quantities, whereas U_j, v_j, and n_j are the amplitudes of oscillations at the jth harmonic; c.c. denotes the complex conjugate. With no external bias applied to the transistor's channel, employing a functional dependence between charge and voltage oscillations given by $n_1 = (\partial\bar{n}/\partial\bar{U})U_1$, and approximating to the first order of V_a, (1) and (2) reduce to

$$i\omega v_1 + \frac{e}{m}\frac{\partial U_1}{\partial x} + \frac{v_1}{\tau} = 0 \quad (8)$$

$$i\omega \frac{\partial \bar{n}}{\partial \bar{U}} U_1 + \bar{n}\frac{\partial v_1}{\partial x} = 0. \quad (9)$$

Now, by solving (8) for v_1 and using it for (9), we obtain a simple second-order differential equation, which describes the oscillations of the channel potential

$$\frac{\partial^2 U_1}{\partial x^2} + k^2 U_1 = 0. \tag{10}$$

Alternatively, employing the relation $n_1 = (\partial \bar{n}/\partial \bar{U})U_1$, (10) describes density waves. Here, k is defined as the complex quantity

$$k = \frac{\omega}{s}\sqrt{1 - \frac{i}{\omega\tau}} \tag{11}$$

and s is the phase velocity of the density waves

$$s = \sqrt{\frac{e}{m}\bar{n}\frac{\partial \bar{U}}{\partial \bar{n}}}. \tag{12}$$

The solution of (10) has the general form $C_1 e^{ikx} + C_2 e^{-ikx}$ with constants C_1 and C_2 being defined by the boundary conditions. These reflect the coupling scheme of Fig. 2, with the terahertz signal being coupled to the drain contact, and the source and gate contacts being ac shunted. Hence, the solutions for the amplitudes of both the local channel potential and the velocity oscillations have to fulfill the following boundary conditions: no oscillations at the source terminal ($x = 0$), i.e., $U_1(0) = 0$, and the full swing of the potential at the drain ($x = L$). Note, however, that the terahertz signal on the drain counteracts the gate voltage [see (4)]; hence, $U_1(L) = -V_a$. The resulting amplitudes of the channel potential and the velocity exhibit the following form:

$$\left\{ U_1 = -V_a \frac{\sin kx}{\sin kL}, \quad v_1 = \frac{\omega e V_a}{iks^2 m}\frac{\cos kx}{\sin kL} \right\}. \tag{13}$$

In this case, we obtain the following channel impedance as the drain voltage divided by the drain current:

$$Z_d = \frac{U_1}{v_1 e \bar{n} W} = \frac{iks^2 m}{\omega e^2 \bar{n} W}\tan kL. \tag{14}$$

In the QS limit, with $\tan kL \approx kL$ and $k \approx s^{-1}\sqrt{\omega/i\tau}$, the following QS resistance of the unbiased channel is derived:

$$R_{d,\mathrm{QS}} = \frac{L}{e\bar{n}\mu W} = \frac{L}{\mu\eta V_T C_{\mathrm{ox}} W \ln\left(1 + \frac{1}{2}e^{(V_G - V_{\mathrm{th}})/\eta V_T}\right)}. \tag{15}$$

In the regime of distributed resistive mixing, with $|kL| > 1$ and $\omega\tau < 1$, hence, $\tan kL \approx -i$, the impedance of the channel can be approximated as follows:

$$Z_{d,\mathrm{dis}} \approx \frac{ks^2 m}{\omega e^2 \bar{n} W} \approx \sqrt{\frac{R_{d,\mathrm{QS}}\left(1 + 2e^{-(V_G - V_{\mathrm{th}})/\eta V_T}\right)}{i\omega C_{\mathrm{ox}} W L}}. \tag{16}$$

V. TERAHERTZ SIGNAL RECTIFICATION

In order to describe rectification phenomena, we expand (1) and (2) using (5)–(7) and retain all stationary and time-independent terms to the second order of V_a

$$\frac{d}{dx}\left(\frac{e}{m}\bar{U} + \frac{v_1 v_1^*}{4}\right) + \frac{\bar{v}}{\tau} = 0 \tag{17}$$

$$\frac{d}{dx}\left(s^2\bar{v} + \frac{e}{m}\frac{v_1 U_1^* + v_1^* U_1}{4}\right) = 0. \tag{18}$$

The star denotes complex conjugation. For an unbiased channel, the following stationary velocity is obtained:

$$\bar{v} = -\frac{e}{m}\frac{v_1 U_1^* + v_1^* U_1}{4s^2}. \tag{19}$$

Now, using (17), the induced detector signal $\Delta U = U(L) - U(0)$ can be found from

$$\Delta U = -\frac{m}{e}\frac{v_1 v_1^*}{4}\Big|_{x=0}^{x=L} - \frac{m}{e\tau}\int_0^L \bar{v}\,dx = \frac{e}{m}\frac{V_a^2}{4s^2}f(\omega) \tag{20}$$

where the dimensionless efficiency factor $f(\omega)$ for drain feeding and ac-shorted source–gate contacts (f_{short}) is defined as follows:

$$f_{\mathrm{short}} = -\left(1 + \frac{2\omega\tau}{\sqrt{1 + (\omega\tau)^2}}\frac{\sinh^2 k_2 L - \sin^2 k_1 L}{\cosh^2 k_2 L - \cos^2 k_1 L}\right). \tag{21}$$

The real and imaginary parts of $k = k_1 - ik_2$ are given by

$$k_{1,2} = \frac{\omega}{s\sqrt{2}}\sqrt{\sqrt{1 + \frac{1}{\omega^2\tau^2}} \pm 1}. \tag{22}$$

Here, the "+" sign refers to k_1 and the "−" sign refers to k_2.

Fig. 4(a) illustrates the characteristic device-impedance values of an ac-shorted circuit (14), and Fig. 4(b) presents the resulting efficiency factor f_{short} in comparison with the efficiency factor for an ac-open case (taken from [3, eq. (24)]). For the quantitative calculations of Fig. 4, we use the device parameters taken from the model fit with (4). We additionally show results for a carrier mobility of 330 cm^2/V · s, which is commonly cited in the literature as typical for Si of comparable doping.

We first focus on the efficiency factor $|f_{\mathrm{short}}|$ of (21) shown in Fig. 4(b). The first striking feature of its frequency dependence is that it has unity value over a very broad frequency range. Rectification at low frequencies can be well understood as classical resistive self-mixing of the applied signal with itself. Without ac shunting, as described by Dyakonov and Shur, mixing vanishes, as indicated in Fig. 4(b) by the open symbols. For ac shunting, the device operates as a single lumped element; the reactance increases with frequency. However, this picture breaks down when $\mathrm{Re}\,kL \geq 1$, i.e., when the frequency of oscillations exceeds $\omega \geq 2s^2\tau/L^2$. The frequency boundary given by the "=" sign in this expression is marked in Fig. 4(b). This limit also demarks the maximum of the reactance. The mode of device operation changes here from resistive self-mixing (white background color) to the so-called distributive-resistive mixing (green background color in online version) and the smooth transition of regimes is indicated. The transistor can be described as a distributed RC circuit and a waveguide picture applies [14], [15]. It can be derived from the Dyakonov–Shur equations neglecting the first two terms of (1). In this regime, both the resistance and reactance have a frequency dependence of the form $\sim\sqrt{1/\omega}$ [see Fig. 4(a)]. The value of $|f_{\mathrm{short}}|$ remains unity in this regime.
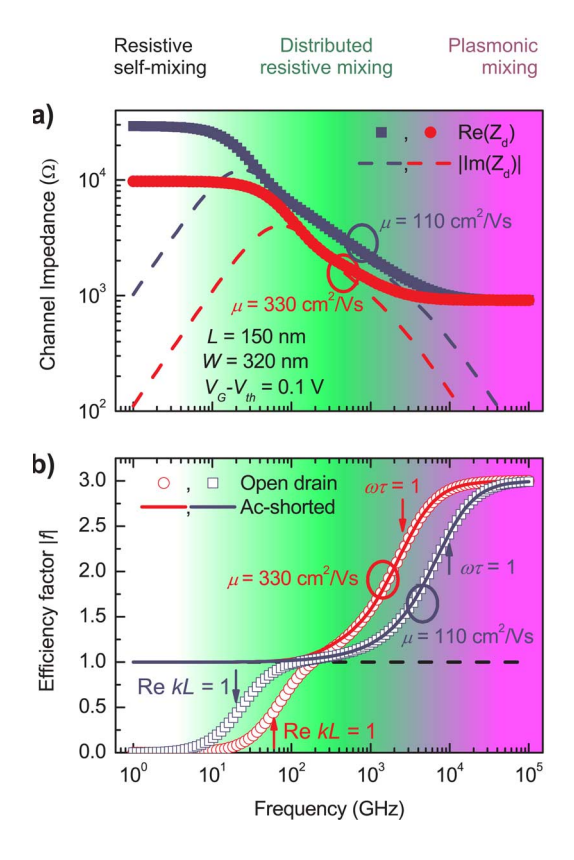
Fig. 4. (a) Frequency dependence of the resistance and reactance according to (14). Simulation results are given for two different values of the electron mobility: red color (in online version) corresponds to the literature-specified $330\ \mathrm{cm^2/V \cdot s}$, blue (in online version) to the mobility value of $110\ \mathrm{cm^2/V \cdot s}$ extracted from the measurements (compare Fig. 4). (b) Frequency dependence of the detection efficiency factor f for drain coupling depending on the boundary conditions: open symbols correspond to ac open [3], lines to ac-short conditions (21), red and blue colors (in online version) encode different mobility values as specified above. Vertical arrows indicate positions where $\mathrm{Re}\ kL = 1$, as well as $\omega\tau = 1$, defining the transitions between classical resistive mixing (white background color), distributed resistive mixing (green background color in on-line version), and plasmonic mixing (pink background color in online version). Dashed line: classical-resistive-mixing limit of distributed resistive mixing, as described in [14]; the value is used as reference value and set to unity.

With rising frequency, $|f_{\mathrm{short}}|$ slowly increases. The *RC*-waveguide model does not account for this rise, but rather predicts unity value, as illustrated by the dashed line in Fig. 4(b). The rise is a consequence of the contribution to mixing by the first two terms of (1), which can no longer be neglected at higher frequencies. Depending in detail on carrier mobility and the length of the channel, the onset of this new regime, indicated by pink background color (in online version), which follows upon the distributed resistive-mixing regime, is found at comparatively low frequencies, long before the condition $\omega\tau = 1$ for one scattering event per plasmon period is fulfilled. This aspect should be even more pronounced for material systems with much higher mobility such as GaN-, GaAs-, or InP-based HEMTs of comparable channel length.

When the condition $\omega\tau \geq 1$ is fulfilled, one can speak of fully developed plasmonic mixing. The absolute value of the efficiency factor continuously increases with frequency. When the last term (the scattering term) in (1) becomes less important relative to the first (time derivative) term, $|f_{\mathrm{short}}|$ asymptotically approaches the value of 3 [see Fig. 4(b)] for the long-channel

case considered here [3], and the resistance becomes constant [see Fig. 4(a)].

With the expressions given before in this paper, we can now also specify the responsivity to be expected from our detectors

$$\Re_{I,\mathrm{QS}} = \frac{\dfrac{\Delta U}{R_{d,\mathrm{QS}}}}{\dfrac{V_a^2}{2R_{d,\mathrm{QS}}}}$$
$$= \frac{e}{m}\frac{1}{2s^2}$$
$$= \frac{1}{2\eta V_T \ln\left(1+\dfrac{1}{2}e^{(V_G-V_{\mathrm{th}})/\eta V_T}\right)\left(1+2e^{-(V_G-V_{\mathrm{th}})/\eta V_T}\right)}. \tag{23}$$

Equation (23) gives a term for the current responsivity $\Re_I$ in the QS limit in similar terms as is possible for diode-based rectifiers. The expression is derived by converting the detected voltage to a current flowing through the channel. The conversion is achieved with the expression for the impedance for the case that the channel is dc shorted by connecting the detector to a current or transimpedance amplifier. In the deep subthreshold limit ($V_G \ll V_{\mathrm{th}}$), the responsivity $\Re_{I,\mathrm{QS}}$ approaches the ideal value of $1/2\eta V_T \approx 20$ A/W at room temperature, which is the same as for diode-based rectifiers [27]. In practical terms, this value is not reachable with FETs due to the very high channel impedance in the subthreshold regime. Yet, at the typical operation point of $V_G - V_{\mathrm{th}} \approx 0.1$ V, the impedance is on the order of several tens of kΩ, and then $\Re_{I,\mathrm{QS}} \approx 1/4\eta V_T \approx 10$ A/W at room temperature.

When investigating the high-frequency performance more precisely, one has to take into account that the real part of the impedance is lower than the QS value [see Fig. 4(a)]. One obtains the following expression, when conjugate matching is fulfilled:

$$\Re_{I,\mathrm{matched}} = \frac{\dfrac{\Delta U}{R_{d,\mathrm{QS}}}}{\mathrm{Re}\left(\dfrac{V_a^2}{2Z_d}\right)} = \Re_{I,\mathrm{QS}}\frac{f(\omega)}{\mathrm{Re}Z_d^{-1}R_{d,\mathrm{QS}}}. \tag{24}$$

Since FET detectors are coupled to antennas and we refer the responsivity to the power P_{in}, which would be interacting with an ideal (lossless) and impedance matched antenna, rather than the power $\mathrm{Re}\{V_a^2/2Zd\}$, which is delivered to the transistor, we use

$$\mathrm{Re}\left\{\frac{V_a^2}{2Z_d}\right\} = P_{\mathrm{in}}\frac{\varepsilon}{2}\frac{4\mathrm{Re}Z_d\mathrm{Re}Z_{\mathrm{ant}}}{|Z_d+Z_{\mathrm{ant}}|^2}. \tag{25}$$

Here, the factor $\varepsilon/2$ takes into account the power dissipated in the antennas internal impedance, as well as the power dissipated as heat. The last factor describes the impedance mismatch between the antenna feed-point impedance Z_{ant} and the transistor impedance Z_d (see [28]). The following prediction for the optical detector responsivity in the unmatched case is reached:

$$\Re_I = \frac{\dfrac{\Delta U}{R_{d,\mathrm{QS}}}}{P_{\mathrm{in}}} = \Re_{I,\mathrm{QS}}f(\omega)\frac{\mathrm{Re}Z_{\mathrm{ant}}}{R_{d,\mathrm{QS}}}\frac{\varepsilon}{2}\left|\frac{2Z_d}{Z_d+Z_{\mathrm{ant}}}\right|^2. \tag{26}$$

Thus far, the device model only includes the channel impedance. For more accurate treatment, additional parasitic effects have to be included. We limit our treatment to an empirical parasitic capacitance C_{par} by replacing the device impedance with $Z_d \rightarrow 1/(1/Z_d + j\omega C_{par})$. More details on this effect are discussed later. Finally, the NEP can be derived as

$$\text{NEP} = \frac{\sqrt{4k_B T}}{\sqrt{R_{d,QS}} \Re_I}. \quad (27)$$

For cold MOSFETs (without drain bias), the dominant noise source is thermal Johnson noise, as has been shown for similar devices in [19], and has also been experimentally verified for the LFoundry transistors, which have been used in the experimental part.

VI. RESULTS

With the expressions given above, we can now quantitatively compare measured data with the results of model calculations. We start with a detector pixel connected to a patch antenna with the resonance at about 583 GHz. The procedure to determine the intensity profile of the terahertz beam at the detection plane has been described elsewhere [29]. It is based on integrating the incoming radiation signal over the whole terahertz beam area by mapping the intensity distribution of the beam via raster scanning of an individual detector pixel, and comparing the resulting integrated signal with the absolute power value measured with a calibrated power meter. Since any responsivity estimate relies on an assumption for the area of the detector, for practical reasons, one often takes the pitch of neighboring antennas of the focal-plane array as detector area. Due to chip size constraints, some pixels have not been arranged in a focal-plane array configuration, for which we use simulated effective areas.

In Fig. 5, we present the dependence of the detected current on gate voltage for a low-frequency-modulated terahertz signal (open circles) and an electrically applied 6-MHz signal (solid line), both measured in the small-signal regime. For comparative purposes, the amplitude of the terahertz response has been normalized to the electrical response value at a gate bias voltage of 0.6 V. Note that the responsivities show a near-identical dependence on gate bias because, in both cases, the amplitude of the oscillations was independent from bias conditions. This was the case because both the 50-Ω impedance of the electrical source and the simulated antenna impedance of 236 Ω are much lower than the real part of the detector impedance [see Fig. 4(a)] over the whole bias range.

Using (23)–(27), we are then able to estimate a possible NEP in QS and distributed resistive mixing regimes shown in Fig. 5 with the dotted and short dashed lines, correspondingly. Note that because of the two-transistor configuration of the detector, which is shown in Fig. 2, the low-frequency resistance is only half of the channel resistance of a single device. Results indicate that at practical operation point (device impedance controlled by gate bias), the NEP of high-frequency impedance matched detectors can be as low as 2 pW/$\sqrt{\text{Hz}}$. Similar performance is also expected in detectors based on high mobility transistors [30]. Experimentally determined NEP at the resonance frequency is shown in Fig. 5 with red diamonds (in online version). For this device, its minimum reaches ~46 pW/$\sqrt{\text{Hz}}$. The measured data
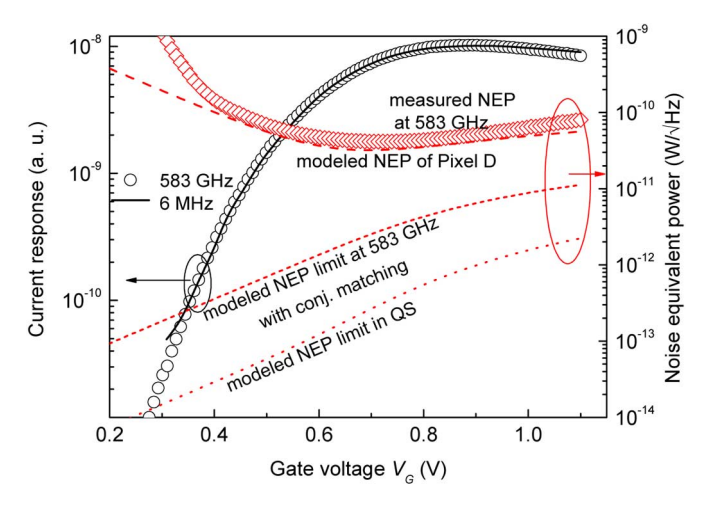

Fig. 5. Comparing the gate-bias-dependent detector performance of a single detector device at 6 MHz (lines) and 583 GHz (symbols). In black, the close agreement of the current response in the QS and the terahertz regime is shown. Red diamonds (in online version) represent the measured optical NEP. The red lines (in online version) show the theoretically achievable limit (conjugate impedance matching) in the QS regime (dotted) and distributed-resistive-mixing regime (short dashed), as well as the modeled NEP including impedance mismatch (dashed).
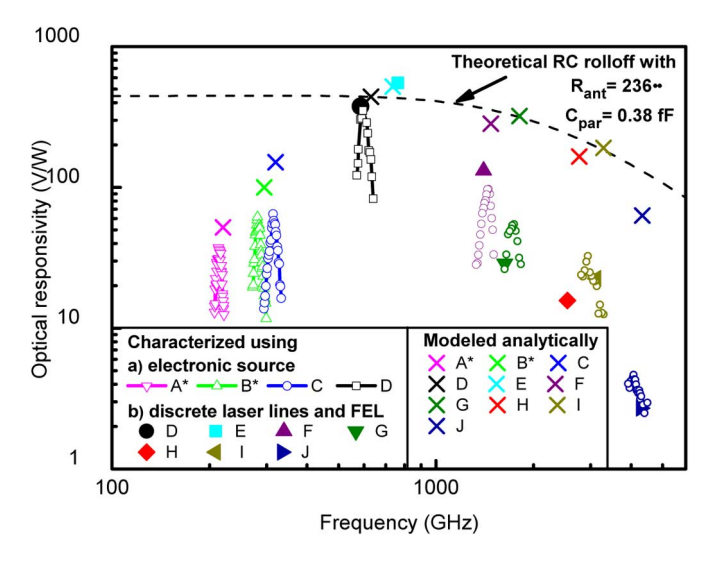

Fig. 6. Optical responsivity of detectors designed for discrete frequencies. Up to 600-GHz detectors have been characterized using electronic sources. Above 595 GHz, we used discrete lines of a CO_2-pumped molecular gas laser and a pulsed free-electron laser. Crosses show the modeled values. The dashed line indicates simulated roll-off due to parasitic capacitance.

compares well with modeled performance of the unmatched case. The deviation below 0.4 V is due to loading effects. The same pixel on another die, which is used in the characterization below, shows a slightly better minimum NEP of 42 pW/$\sqrt{\text{Hz}}$.

Finally, in Fig. 6, we present voltage responsivity values for otherwise identical detectors, but connected to different patch antennas. For characterizations at 600 GHz and below, we used electronic multiplier-based sources. Detectors at and above 585 GHz have been characterized with continuous-wave radiation from discrete lines of a CO_2-pumped molecular gas laser. Independently four pixels above 1 THz have been characterized with free electron laser source FELBE at the Helmholtz-Zentrum Dresden-Rossendorf, Dresden, Germany.

The pulse length was up to few 10 ps, depending on the frequency. In both cases, samples were subjected to a broad Gaussian beam for which the power density was previously determined.

Starting from the lower frequency side, performance of resonant detectors strongly increase. Although an ideal patch antenna should perform similarly at this frequency range, the simulations show that the limited conductivity of metal layers result in substantial reduction of both antenna efficiency and impedance. On the higher frequency side, detectors at 0.595, 0.763, 1.4, 1.75, 2.9, and 4.1 THz show optical responsivities of 350, 550, 132, 55, 30, and 4.6 V/W, respectively. The crosses show the modeled values. While there is a good agreement between model and measured data below 1 THz, the performance roll-off is slightly stronger than modeled above 1 THz. The dashed line indicates modeled roll-off limited by the time constant set from an assumed antenna impedance of $R_{\mathrm{ant}} = 236\ \Omega$ and parasitic capacitance $C_{\mathrm{par}} = 0.38$ fF and also taking the increase of mixing efficiency in this frequency range into account. The parasitic capacitance includes the junction, overlap, and fringe capacitance and are considered to be connected in parallel to the transistor channel. By implementing detectors with different channel width at 570 GHz and characterizing the responsivity roll-off with gate width, we estimated a parasitic capacitance of $C_{\mathrm{par}} = 0.38$ fF. We assumed that the capacitance scale linearly with channel width. We also took into account that threshold voltage U_{th} and nonideality η change with gate width within our theoretical description used. Despite the somewhat stronger roll-off than indicated, outstanding performance can be achieved as demonstrated by the 2.9-THz result, where a responsivity of 30 V/W and a NEP value of $487\mathrm{pW}/\sqrt{\mathrm{Hz}}$ are reached, respectively.

VII. CONCLUSION

In conclusion, we have integrated FET-based detectors for operation at discrete frequencies spanning from 0.2 to 4.3 THz using a commercial 0.15-μm CMOS process technology. Detectors utilize a novel design in which the signal from the patch antenna is applied between the drain and source terminals. This design enables estimation of detector performance from rectification of electrically applied low-frequency oscillations. We present a unified model based on hydrodynamic transport description to account for rectification efficiency and device impedance over the full range of gate bias and frequencies and apply it for different boundary conditions. The model is supported by experimental results at 6 MHz and 583 GHz and good agreement is achieved between model and measurements. Our results allow estimating the limiting values for room-temperature NEP for detection at 600-GHz radiation of $2\ \mathrm{pW}/\sqrt{\mathrm{Hz}}$ for a practical gate bias of 0.7 V. When antenna efficiency and impedance mismatch are taken into account, the derived model is in good agreement at 583 GHz with the measured data. Here, a minimum value of $46\ \mathrm{pW}/\sqrt{\mathrm{Hz}}$ is reached. Detectors with scaled antenna designs have been characterized up to 4.3 THz. In particular, detectors at 0.595, 0.763, 1.4, 1.75, 2.9, and 4.1 THz show optical responsivities of 350, 550, 132, 55, 30, and 4.6 V/W, respectively. Accounting for the estimate of total parasitic capacitance and uncertainty in

matching of antenna resonant frequencies, our results show that the detection concept persists deep into the terahertz gap. The CMOS metal stack also literally leaves room for improvement by relaxing design constraints at higher frequencies. With this in mind, intrinsically fast electronic components seem feasible deep in the terahertz gap, which not only would render possible single color cameras, but also spectroscopic sensors based on frequency-selective antennas tailored for various frequencies.

REFERENCES

[1] S. Boppel, A. Lisauskas, D. Seliuta, L. Minkevicius, L. Kasalynas, G. Valusis, V. Krozer, and H. G. Roskos, "CMOS integrated antenna-coupled field-effect-transistors for the detection of 0.2 to 4.3 THz," in *12th IEEE Silicon Monolithic Integr. Circuits RF Syst. Top. Meeting*, Santa Clara, CA, 2012, pp. 1–3.
[2] A. V. Chaplik, "Absorption and emission of electromagnetic waves by two-dimensional plasmons," *Surface Sci. Rep.*, vol. 5, no. 7, pp. 289–335, 1985.
[3] M. Dyakonov and M. Shur, "Detection, mixing, and frequency multiplication of terahertz radiation by two-dimensional electronic fluid," *IEEE Trans. Electron. Devices*, vol. 43, no. 3, pp. 380–387, Mar. 1996.
[4] J.-Q. Lu, M. S. Shur, J. L. Hesler, L. Sun, and R. Weikle, "Terahertz detector utilizing two-dimensional electronic fluid," *IEEE Electron Device Lett.*, vol. 19, no. 10, pp. 373–375, Oct. 1998.
[5] S. Nadar, H. Videlier, D. Coquillat, F. Teppe, M. Sakowicz, N. Dyakonova, W. Knap, D. Seliuta, I. Kašalynas, and G. Valušis, "Room temperature imaging at 1.63 and 2.54 THz with field effect transistor detectors," *J. Appl. Phys.*, vol. 108, 2010, Art. ID 054508.
[6] Y. F. Sun, J. D. Sun, Y. Zhou, R. B. Tan, C. H. Zeng, W. Xue, H. Qin, B. S. Zhang, and D. M. Wu, "Room temperature GaN/AlGaN self-mixing terahertz detector enhanced by resonant antennas," *Appl. Phys. Lett.*, vol. 98, 2011, Art. ID 252103.
[7] W. Knap, Y. Deng, S. Rumyantsev, and M. S. Shur, "Resonant detection of subterahertz and terahertz radiation by plasma waves in submicron field-effect transistors," *Appl. Phys. Lett.*, vol. 81, pp. 4637–4639, 2002.
[8] X. G. Peralta, S. J. Allen, M. C. Wanke, N. E. Harff, J. A. Simmons, M. P. Lilly, J. L. Reno, P. J. Burke, and J. P. Eisenstein, "Terahertz photoconductivity and plasmon modes in double-quantum-well field-effect transistors," *Appl. Phys. Lett.*, vol. 81, pp. 1627–1629, 2002.
[9] G. C. Dyer, S. Preu, G. R. Aizin, J. Mikalopas, A. D. Grine, J. L. Reno, J. M. Hensley, N. Q. Vinh, A. C. Gossard, M. S. Sherwin, S. J. Allen, and E. A. Shaner, "Enhanced performance of resonant sub-terahertz detection in a plasmonic cavity," *Appl. Phys. Lett.*, vol. 100, no. 8, 2012, Art. ID 083506.
[10] V. V. Popov, G. M. Tsymbalov, D. V. Fateev, and M. S. Shur, "Higher-order plasmon resonances in GaN-based field-effect-transistor arrays," *Int. J. High Speed Electron. Syst.*, vol. 17, pp. 557–566, 2007.
[11] G. C. Dyer, G. R. Aizin, J. L. Reno, E. A. Shaner, and S. J. Allen, "Novel tunable millimeter-wave grating-gated plasmonic detectors," *IEEE J. Sel. Topics Quantum Electron.*, vol. 17, no. 1, pp. 85–91, Jan.–Feb. 2011.
[12] R. Tauk, F. Teppe, S. Boubanga, D. Coquillat, W. Knap, Y. M. Meziani, C. Gallon, F. Boeuf, T. Skotnicki, T. Skotnicki, C. Fenouillet-Beranger, D. K. Maude, S. Rumyantsev, and M. S. Shur, "Plasma wave detection of terahertz radiation by silicon field effects transistors: Responsivity and noise equivalent power," *Appl. Phys. Lett.*, vol. 89, 2006, Art. ID 253511.
[13] W. Knap, V. Kachorovskii, Y. Deng, S. Rumyantsev, J.-Q. Lu, R. Gaska, M. S. Shur, G. Simin, X. Hu, M. A. Khan, C. A. Saylor, and L. C. Brunel, "Nonresonant detection of terahertz radiation in field effect transistors," *J. Appl. Phys.*, vol. 91, no. 11, pp. 9346–9353, 2002.
[14] A. Lisauskas, U. Pfeiffer, E. Öjefors, P. H. Bolívar, D. Glaab, and H. G. Roskos, "Rational design of high-responsivity detectors of terahertz radiation based on distributed self-mixing in silicon field-effect transistors," *J. Appl. Phys.*, vol. 105, 2009, Art. ID 114511.
[15] E. Öjefors, U. R. Pfeiffer, A. Lisauskas, and H. G. Roskos, "A 0.65 THz focal-plane array in a quarter-micron CMOS process technology," *IEEE J. Solid-State Circuits*, vol. 44, no. 7, pp. 1968–1976, Jul. 2009.
[16] E. Öjefors, N. Baktash, Y. Zhao, R. A. Hadi, H. Sherry, and U. R. Pfeiffer, "Terahertz imaging detectors in a 65-nm CMOS SOI technology," in *IEEE Eur. Solid-State Circuits Conf.*, Seville, Spain, Sep. 2010, pp. 486–489.

[17] F. Schuster, D. Coquillat, H. Videlier, M. Sakowicz, F. Teppe, L. Dussopt, B. Giffard, T. Skotnicki, and W. Knap, "Broadband terahertz imaging with highly sensitive silicon CMOS detectors," *Opt. Exp.*, vol. 19, no. 8, pp. 7827–7827, Apr. 2011.

[18] S. Boppel, A. Lisauskas, V. Krozer, and H. G. Roskos, "Performance and performance variations of sub-1 THz detectors fabricated with 0.15-μm CMOS foundry process," *Electron. Lett.*, vol. 47, no. 11, pp. 661–661, 2011.

[19] S. Boppel, A. Lisauskas, A. Max, V. Krozer, and H. G. Roskos, "CMOS detector arrays in a virtual 10-kilopixel camera for coherent terahertz real-time imaging," *Opt. Lett.*, vol. 37, no. 4, pp. 536–536, Feb. 2012.

[20] H. Sherry, J. Grzyb, Y. Zhao, R. A. Hadi, A. Cathelin, A. Kaiser, and U. R. Pfeiffer, "A 1 kpixel CMOS camera chip for 25 fps real-time terahertz imaging applications," in *Proc. IEEE Int. Solid-State Circuits Conf.*, 2012, pp. 252–254.

[21] A. Lisauskas, S. Boppel, M. Saphar, V. Krozer, L. Minkevičius, D. Seliuta, I. Kašalynas, V. Tamošiunas, G. Valušis, and H. G. Roskos, "Detectors for terahertz multi-pixel coherent imaging and demonstration of real-time imaging with a 12 × 12-pixel CMOS array," *Proc. SPIE*, vol. 8496, pp. 84960J–84960J-9, 2012.

[22] A. Lisauskas, S. Boppel, J. Matukas, V. Palenskis, L. Minkevicius, G. Valusis, P. Haring-Bolivar, and H. G. Roskos, "Terahertz responsivity and low-frequency noise in biased silicon CMOS detectors," *Appl. Phys. Lett.*, 2012, submitted for publication.

[23] J. D. Sun, Y. F. Sun, D. M. Wu, Y. Cai, H. Qin, and B. S. Zhang, "High-responsivity, low-noise, room-temperature, self-mixing terahertz detector realized using floating antennas on a GaN-based field-effect transistor," *Appl. Phys. Lett.*, vol. 100, no. 1, 2012, Art. ID 013506.

[24] M. Shur, T. Fjeldly, T. Ytterdal, and K. Lee, "Unified MOSFET model," *Solid State Electron.*, vol. 35, no. 12, pp. 1795–1802, 1992.

[25] M. Abramowitz and I. A. Stegun, *Handbook of Mathematical Functions: With Formulas, Graphs, and Mathematical Tables*. New York: Dover, 1972.

[26] Y. P. Tsivids, *Operation and Modeling of the MOS Transistor*. New York: McGraw-Hill, 1999.

[27] C. Sydlo, O. Cojocari, D. Schönherr, T. Goebel, P. Meissner, and H. L. Hartnagel, "Fast THz detectors based on InGaAs Schottky diodes," *Frequenz*, vol. 62, pp. 107–110, 2008.

[28] S. J. Orfanidis, *Electromagnetic Waves and Antennas*. New Brunswick, NJ: Rutgers Univ. Press, 2008.

[29] A. Lisauskas, D. Glaab, H. G. Roskos, E. Oejefors, and U. R. Pfeiffer, "Terahertz imaging with Si MOSFET focal-plane arrays," in *Proc. SPIE*, San Jose, CA, 2009, Art. ID 72150J.

[30] S. Preu, S. Kim, R. Verma, P. G. Burke, M. S. Sherwin, and A. C. Gossard, "An improved model for non-resonant terahertz detection in field-effect transistors," *J. Appl. Phys.*, vol. 111, no. 2, 2012, Art. ID 024502.

Martin Mundt was born in Görlitz, Germany, in 1990. He is currently working toward the Bachelor's degree in physics at Goethe-Universität Frankfurt, Frankfurt, Germany.

He is currently with the Ultrafast Spectroscopy and Terahertz Physics GroupGoethe-Universität Frankfurt. His fields of interest include plasma effects and the physics of field-effect transistor (FET) detection.

Dalius Seliuta received the M.S. degree in radio physics and electronics from Vilnius University, Vilnius, Lithuania, in 1991, and the Ph.D. degree in solid-state physics from the Semiconductor Physics Institute, Vilnius, Lithuania, in 1998.

Since 2003, he has been a Senior Research Associate with the Center for Physical Sciences and Technology, Vilnius, Lithuania, and since 2004, an Associate Professor with Vilnius Gediminas Technical University, Vilnius, Lithuania. He has coauthored 100 scientific publications. His research interests are quantum semiconductor structures, metamaterial devices, nanoscale terahertz detectors, and carbon nanotube structures.

Linas Minkevičius, photograph and biography not available at time of publication.

Irmantas Kašalynas (M'09) was born in Varéna, Lithuania. He received the B.S. degree in electrical engineering from Vilnius Technical University, Vilnius, Lithuania, in 1995, and the M.S. and Ph.D. degrees in physics from Vilnius University, Vilnius, Lithuania, in 1997, and 2004, respectively.

From 2000 to 2004, he was with the Optoelectronics Group, Inhomogeneous Structures Laboratory, Semiconductor Physics Institute, Vilnius, Lithuania, where, since 2006, he has been a Research Associate with the Terahertz Electronics and Terahertz Photonics Group. In 2005, he was a Postdoctoral Fellow with the Terahertz Imaging Group, Faculty of Applied Science, Delft University of Technology, Delft, The Netherlands. His current research interests include compact room-temperature terahertz and subterahertz radiation detectors and sources, passive filters, and plasmon resonance devices.

Sebastian Boppel was born in Preetz, Germany, in 1982. He received the Physics degree from the University of Heidelberg, Heidelberg, Germany, in 2008, and is currently working toward the Ph.D. degree in physics at Goethe-Universität Frankfurt, Frankfurt, Germany.

He is currently with the Ultrafast Spectroscopy and Terahertz Physics Group, Goethe-Universität Frankfurt, where he is involved in the area of CMOS-transistor-based terahertz detection.

Alvydas Lisauskas received the Diploma degree in physics from Vilnius University, Vilnius, Lithuania, in 1995, and the Ph.D. degree from the Royal Institute of Technology, Stockholm, Sweden, in 2001.

From 2001 to 2002, he was a Senior Researcher with the Semiconductor Physics Institute, Vilnius, Lithuania. Since 2002, he has been a member of the Ultrafast Spectroscopy and Terahertz Physics Group, Goethe-Universität Frankfurt, Frankfurt, Germany, where he is involved with fundamental aspects of novel semiconductor devices for terahertz applications.

Gintaras Valušis received the Diploma degree from the Faculty of Physics and Ph.D. degree from Vilnius University, Vilnius, Lithuania, in 1985 and 1992, respectively.

From 1995 to 1996, he was a Postdoctoral Researcher with the Institute of Applied Photo Physics, Dresden University of Technology. In 2000, he was an Alexander von Humboldt Fellow with the Physics Institute, J. W. Goethe University, Frankfurt, Germany. He is currently a Deputy Director for development with the Center for Physical Science and Technology, Head of the Terahertz Photonics Laboratory, and Professor with the Semiconductors Physics Department, Physics Faculty, Vilnius University.

Martin Mittendorff was born in Heilbronn, Germany, in 1979. He studied photonics and image processing and received the Diploma degree from the University of Applied Science, Darmstadt, Germany, in 2010, and is currently working toward the Ph.D. degree at the Helmholtz-Zentrum Dresden-Rossendorf, Dresden, Germany.

His current research interests include ultrafast spectroscopy of graphene, especially in magnetic fields.

Mr. Mittendorff is a member of the German Physical Society (DPG).

Stephan Winnerl was born in 1970. He received the Diploma degree and Ph.D. degree in physics from the University of Regensburg, Regensburg, Germany, in 1996 and 1999, respectively.

For two years, he was a Postdoctoral Member with Forschungszentrum Julich. Since 2002, he has been with the Forschungszentrum Dresden-Rossendorf, Dresden, Germany. His current research interests include ultrafast spectroscopy of semiconductor quantum structures and terahertz research.

Dr. Winnerl is a member of the German Physical Society (DPG).

Viktor Krozer (M'91–SM'03) received the Dipl.-Ing. and Dr.-Ing. degrees in electrical engineering from the Technical University of Darmstadt (TU Darmstadt), Darmstadt, Germany, in 1984 and 1991, respectively.

In 1991, he became a Senior Scientist with TU Darmstadt, where he was involved with high-temperature microwave devices and circuits and submillimeter-wave electronics. From 1996 to 2002, he was a Professor with the Technical University of Chemnitz, Chemnitz, Germany. From 2002 to 2009, he was a Professor with Electromagnetic Systems, DTU Elektro, Technical University of Denmark, Copenhagen, Denmark, and Head of the Microwave Technology Group. Since 2009, he has been the endowed Oerlikon-Leibniz-Goethe Professor for Terahertz Photonics with Goethe-Universität Frankfurt, Frankfurt, Germany. His research areas include terahertz electronics, monolithic microwave integrated circuits, nonlinear circuit analysis and design, device modeling, and remote sensing instrumentation.

Hartmut G. Roskos studied physics at the Technical University of Karlsruhe, Karlsruhe, Germany, and the Technical University of Munich, Munich, Germany. He received the Ph.D. degree from the Technical University of Munich, in 1989. His thesis concerned femtosecond spectroscopy in solid-state physics. He received the Habilitation degree from Rheinisch-Westfaelische Technische Hochschule Aachen, Germany. His thesis was entitled "Coherent Phenomena in Solid-State Physics Investigated by Terahertz Spectroscopy."

He is currently a Professor of physics with Goethe-Universität Frankfurt, Frankfurt, Germany, where he heads the Ultrafast Spectroscopy and Terahertz Physics Group. For two-and-a-half years, he was with AT&T Bell Laboratories, Holmdel, NJ, during which time his research was focused on terahertz phenomena. He later started a terahertz research group with the Institute of Semiconductor Electronics, RWTH Aachen. In 1997, he joined Goethe-Universität Frankfurt, as a Full Professor. The central themes of his group's research are terahertz physics and photonics, terahertz imaging, and the time-resolved optical and terahertz spectroscopy of inorganic semiconductors and organic compounds. In 2005, he spent a sabbatical with the University of California at Santa Barbara, where he was involved with a Bloch-gain terahertz laser. In 2009, OC Oerlikon AG awarded his group a five-year endowed professorship for terahertz photonics. During the winter semester of 2009/2010, he was a Guest Professor with Institute of Laser Engineering, Osaka University, where he performed terahertz spectroscopy on a 1-D organic metal.